Low-CNR inverse synthetic aperture LADAR imaging demonstration with atmospheric turbulence

R. Trahan[*a], B. Nemati[a], H. Zhou[a], M. Shao[a], I. Hahn[a], W. Schulze[a]
[a]Jet Propulsion Laboratory, 4800 Oak Grove Drive, Pasadena, CA, USA 91109

ABSTRACT

An Inverse Synthetic Aperture LADAR (ISAL) system is capable of providing high resolution surface mapping of near Earth objects which is an ability that has gained significant interest for both exploration and hazard assessment. The use of an ISAL system over these long distances often presents the need to operate the optical system in photon-starved conditions. This leads to a necessity to understand the implications of photon and detector noise in the system. Here a Carrier-to-Noise Ratio is derived which is similar to other optical imaging CNR definitions. The CNR value is compared to the quality of experimentally captured images recovered using the Phase Gradient Autofocus technique both with and without the presence of atmospheric turbulence. A minimum return signal CNR for the PGA to work is observed.

Keywords: Inverse Synthetic Aperture LADAR, ISAL, Long-range imaging, Phase Gradient Autofocus, PGA, Range-Doppler imaging, Carrier-to-noise ratio, CNR

1. INTRODUCTION

The progression of range-Doppler radar has led to the development of optical radar systems, LADAR, due to the increased range and cross-range imaging resolution and better active illumination directivity [1, 2]. The system of specific interest here is the Inverse Synthetic Aperture LADAR (ISAL). An ISAL system actively illuminates the moving or rotating target with a chirped laser. The reflection from the target is captured and detected with a sensitive heterodyne detector. This detector simultaneously yields the intensity and phase of the return signal [3, 4]. The frequency of the intensity information gives the range to a scatterer on the target, and the phase progression resulting from a small Doppler shift gives the velocity of a scatterer on the target. The intensity and phase information is used to "focus" or reconstruct a projection of the three-dimensional target object into a two-dimensional topographical map. This LADAR method is particularly well suited for imaging small near-Earth bodies because most have a nearly constant rotational velocity and many produce sizable retro-reflections [5, 6].

In the assessment of the quality of a return signal, the carrier-to-noise ratio (CNR) is a common metric [7, 8, 9]. Here we wish to determine the consistency in the relationship between the CNR value and the quality of the final image returned from the field-standard Phase Gradient Autofocus (PGA) algorithm without the assumption that the detector is photon limited as was made in [7]. Additionally, we wish to assess the performance of PGA at low signal levels opposed to the discussion in [10] where a high CNR is considered. The intention here is to find a metric which will predict whether PGA will be able to produce a proper image. The basis of this study is empirical data, not simulation.

We wish to observe the relationship between CNR and the quality of an image. For this comparison the contrast of the image is used as the quality metric. To begin this study the definitions of CNR and contrast must be meticulously stated and thoroughly understood. Next, an overview of an experimental ISAL testbed is presented. This testbed is used to systematically assess the correlation between the quality of an image from the PGA algorithm with the corresponding CNR value of the signal. We show that ISAL data from two targets can have the same CNR value, but some can be focused into an image while others cannot. This results in a CNR and analogously a number of photons per range-bin threshold which is necessary but not sufficient for the PGA algorithm to return the desired result. The addition of atmospheric turbulence in the beam path is shown to further increases this threshold.

*Russell.Trahan@jpl.nasa.gov

2. DERIVATION OF THE DETECTION MODEL

The CNR can be simply stated as an estimate of the carrier signal strength from the target divided by the standard deviation of that estimate. The definition of CNR, however, must have a rigorous definition of this estimate and standard deviation. To correctly define the estimate and standard deviation, a model of the measurements in the ISAL detector must be derived. This model will give insight into the meaning and proper uses of the CNR quantity. The modeling of the CNR here expands on the discussions in [8, 9] but photon-limited conditions are not assumed resulting in a more generally applicable result. The conceptual definition of CNR being used here is comparable to that used in the telecommunications industry; however, here photon rates are used instead of RF signal power [11, 12].

Consider that the total optical power incident upon a detector is related to the E field integrated over the detector area as

$$P_d = \int_{A_d} \tfrac{1}{2} \left| E \exp\left(2\pi i f t + i\varphi\right) \right|^2 dA \tag{1}$$

where A_d, f, t, and φ are the detector area, frequency, time, and phase of the field. The amplitude E is chosen such that

$$P_d = \tfrac{1}{2} A_d \bar{E}^2 \tag{2}$$

where $\bar{E}$ is the average amplitude over the detector area. Therefore, under this notation

$$\bar{E}^2 = \frac{2hcN}{\lambda A_d \tau} \tag{3}$$

in which N is the number of photons incident upon the detector in the averaging time τ. This definitions follows the classical notion that there is no fluctuation in the photon rate, i.e. shot noise is not considered [13, 14]. Shot noise and detector noise will be introduced later in this derivation.

In the ISAL system, the laser frequency is chirped such that the waveform in time is $E \exp\left(2\pi i\left(f_0 + \frac{1}{2}\dot{f}t\right)t\right)$. Assume that the local oscillator (LO) of the heterodyne detector follows this waveform, and the waveform of the signal (S) returned from a point target is delayed and phase shifted. The total waveform seen by the detector is thus

$$E_D = E_{LO} \exp\left(2\pi i\left(f_0 + \tfrac{1}{2}\dot{f}t\right)t\right) + E_S \exp\left(2\pi i\left(f_0 \tfrac{1}{2}\dot{f}\left(t+\Delta t\right)\right)\left(t+\Delta t\right) + i\varphi\right) \tag{4}$$

Making use of the notation in Eqs. (1) through (3), the output from the detector due to the field E_D is an electrical current given by

$$\begin{aligned} I_D &= \frac{\eta_d \lambda e}{hc} \int_{A_d} \left\| E_D \right\|^2 dA \\ &= \frac{\eta_d \lambda e}{hc} \left[\tfrac{1}{2} A_d \bar{E}_L^2 + \tfrac{1}{2} A_d \bar{E}_s^2 + A_d \sqrt{\eta_h} \bar{E}_L \bar{E}_s \cos\left(2\pi\Delta f t + \varphi\right) \right] \\ &= \eta_d e \frac{N_L + N_s}{\tau} + 2\eta_d e \frac{\sqrt{\eta_h N_L N_s}}{\tau} \cos\left(2\pi\Delta f t + \varphi\right) \end{aligned} \tag{5}$$

where η_d is the quantum efficiency of the detector, η_h is the heterodyne efficiency, e is the charge of an electron, N_L and N_S are the mean number of LO and signal photons per pulse, and Δf is the beat frequency between the return signal and the LO [9, 13].

The Fourier transform of the photodetector output must be computed to isolate the carrier signal's amplitude from other return signals and other noise contributions. If a pulse is sampled $2M$ times, the Δf DFT frequency element is thus

$$\begin{aligned} D\left(\Delta f\right) &= \frac{\tau}{2M} \sum_{m=0}^{2M-1} 2\eta_d e \frac{\sqrt{\eta_h N_L N_s}}{\tau} \cos\left(2\pi\Delta f t_m + \varphi\right) \exp\left(-2\pi i \Delta f t_m\right) \\ &= \eta_d e \sqrt{\eta_h N_L N_s} \exp\left(i\varphi\right) \end{aligned} \tag{6}$$

The quantity in Eq. (6) is the Fourier transform of the heterodyne signal assuming constant photon rates in the LO and return signal. In reality the detected signal $\tilde{D}(\Delta f)$ is subject to shot noise and detector noise. The exact variances of these noise components will be modeled later, but for now let the shot noise and detector noise have variances σ_{SN}^2 and σ_{NEP}^2 respectively. These two noise sources introduce zero-mean, complex-valued Gaussian noise into the signal such that the detected number of signal photons $\tilde{N}_S$ follows the model [15]

$$\tilde{D}(\Delta f) = \eta_d e \sqrt{\eta_h N_L \tilde{N}_s}\, \exp(i\tilde{\varphi}) = \eta_d e \sqrt{\eta_h N_L N_s}\, \exp(i\varphi) + N\left(0, e^2\sigma_{SN}^2\right) + N\left(0, e^2\sigma_{NEP}^2\right) \tag{7}$$

In this notation, $N(0,\sigma^2)$ indicates a complex-valued, zero-mean Gaussian random variable with a variance of σ^2. To further simplify, the charge of an electron can be divided through to give the non-dimensional form

$$\eta_d \sqrt{\eta_h N_L \tilde{N}_s}\, \exp(i\tilde{\varphi}) = \eta_d \sqrt{\eta_h N_L N_s}\, \exp(i\varphi) + N\left(0, \sigma_{SN}^2\right) + N\left(0, \sigma_{NEP}^2\right) \tag{8}$$

This model of the Fourier transform of the measured photodetector data will be used to define a carrier-to-noise ratio based on estimates of the number of signal and LO photons.

2.1 Mean number of photons per pulse per range-bin

The estimates of N_L and N_S are the results of quantifying the temporal-mean optical power at the photodetector due to the LO and from a single range-bin target respectively. The estimate is based on the mean Power Spectrum Density (PSD) of the voltage measurements from the photodetector during several pulses. Given the j^{th} voltage measurement in the k^{th} pulse, the mean PSD is

$$P_u = \frac{2}{N_P N_V \delta f} \sum_{k=0}^{N_P-1} \left\| \sum_{j=0}^{N_V-1} V_{j,k} \exp\left(-2\pi i \frac{ju}{N_V}\right) \right\|^2, \quad u = [0 \,..\, N_V - 1]. \tag{9}$$

It is worth noting that in the expression shown here the voltage measurements for a single pulse are isolated from the time history using a rectangular window function. The imaging results are improved if a better window such as a Taylor window is used [16]. The rectangle function tends to cause ghost images to appear in the final result because of the side-lobes in the Fourier transform of the rectangle function.

If the range-bin in the positive frequency half of the PSD exists at the index u and the spectral resolution is δf, the total electrical power of the return signal is

$$P_{Sig} = \delta f \left(P_u - \bar{P}\right) \tag{10}$$

where $\bar{P}$ is the mean background in the PSD near the signal peak. Since the measured signal is the result of heterodyne mixing, the heterodyne power is

$$P_{Het} = \frac{\sqrt{2P_{Sig}}}{G_{AC}} \tag{11}$$

in which G_{AC} is the gain of any amplification to the AC voltage signal between the photodetector and the data acquisition. The optical power returned from the target in the range-bin being considered is thus

$$P_{Ret} = \frac{P_{Het}^2}{4P_L} \tag{12}$$

where P_L is the optical power received by the photodetector from the LO. The LO optical power can be determined from the DC voltage signal from the photodetector V_{DC} as

$$P_L = \frac{V_{DC}}{G_{DC}} \tag{13}$$

where G_{DC} is the gain of any amplification to the DC voltage signal between the photodetector and the data acquisition. Defining $E_{Ph} = hc/\lambda$, the average number of local oscillator photons detected per pulse is

$$N_L = \frac{P_L \tau}{E_{Ph}} \tag{14}$$

and the average number of signal photons per pulse in this range-bin is

$$N_S = \frac{P_{Ret} \tau}{E_{Ph}} \tag{15}$$

2.2 Variance of the photon rates

The photon detection rate is corrupted by shot noise and detector noise. The shot noise is described by a two-dimensional Gaussian which corrupts the complex value described by Eq. (6). Shot noise is known to be a Poisson process—the variance is equal to the mean. As a result if the total number of photons detected by the photodetector is $\eta_d(N_L + N_S)$, the width of the Gaussian corrupting the number of detected photons is equal to this quantity. Since the zero-mean two-dimensional Gaussian probability density function is described as

$$f(x) = \frac{1}{2\pi\sigma^2} \exp\left(-\frac{\text{real}(x)^2 + \text{imag}(x)^2}{2\sigma^2} \right) \tag{16}$$

and the variance of this two-dimension Gaussian follows

$$\text{var}\left(f(x)\right) = \text{var}\left(real\left(f(x)\right)\right) + \text{var}\left(imag\left(f(x)\right)\right) = 2\sigma^2, \tag{17}$$

the variance due to shot noise is

$$\sigma_{SN}^2 = \tfrac{1}{2}\eta_d N_L \tag{18}$$

assuming $N_L \gg N_S$.

The detector noise can be quantified by the detector's "noise equivalent power" (NEP). This quantity specifies the electrical power seen over a frequency band at some mean frequency. It is given in units of Watts per root Hertz. In this case the mean frequency is the beat frequency Δf, and the frequency band is the bandwidth of a range element being captured. This range element size is dictated by the range resolution of the detector. Given a detection time τ, the range resolution is

$$\delta r = \frac{c}{2\dot{f}\tau} \tag{19}$$

Converting the range resolution to a frequency resolution, which corresponds to the pulse voltage FFT spectral resolution, in the return heterodyne signal gives

$$\Delta f_{res} = \frac{2\dot{f}\delta r}{c} = \frac{1}{\tau} \tag{20}$$

The NEP is assumed to follow the standard convention as described in [17]. Converting the NEP quantity P_{NE} to a variance of the two-dimensional Gaussian corrupting the number of detected photons per pulse yields

$$\sigma_{NEP}^2 = \frac{1}{2}\left(\frac{P_{NE}\lambda\sqrt{\Delta f_{res}}}{hc}\tau \right)^2 = \frac{P_{NE}^2 \lambda^2 \tau}{2h^2c^2} \tag{21}$$

3. CARRIER-TO-NOISE RATIO DEFINITION

As stated previously, the CNR definition is the ratio of the carrier signal strength to the standard deviation of that estimate. Using the model in Eq. (8), the CNR can be defined as

$$CNR = \frac{\left\langle N_L \tilde{N}_S \right\rangle}{\sqrt{\left\langle N_L^2 \tilde{N}_S^2 \right\rangle - \left\langle N_L \tilde{N}_S \right\rangle^2}} \tag{22}$$

Taking the second statistical moment of Eq. (8) and letting $\varphi = 0$ without loss of generality gives

$$\begin{aligned} \left\langle N_L \tilde{N}_S \right\rangle &= \left\langle N_L N_S \right\rangle + \frac{\left\langle N\left(0,\sigma_{SN}\right)^2 \right\rangle}{\eta_d^2 \eta_h} + \frac{\left\langle N\left(0,\sigma_{NEP}\right)^2 \right\rangle}{\eta_d^2 \eta_h} \\ &= \left\langle N_L N_S \right\rangle + 2\frac{\sigma_{SN}^2 + \sigma_{NEP}^2}{\eta_d^2 \eta_h} \end{aligned} \tag{23}$$

Squaring this equation, as is needed to substitute into the denominator of Eq. (22), yields

$$\left\langle N_L \tilde{N}_S \right\rangle^2 = \left\langle N_L N_S \right\rangle^2 + \frac{4N_L N_S}{\eta_d^2 \eta_h}\left(\sigma_{SN}^2 + \sigma_{NEP}^2\right) + \frac{4}{\eta_d^4 \eta_h^2}\left(\sigma_{SN}^4 + \sigma_{NEP}^4 + 2\sigma_{SN}^2 \sigma_{NEP}^2\right) \tag{24}$$

Taking the fourth statistical moment of Eq. (8) gives

$$\left\langle N_L^2 \tilde{N}_S^2 \right\rangle = \left\langle N_L^2 N_S^2 \right\rangle + \frac{8N_L N_S}{\eta_d^2 \eta_h}\left(\sigma_{SN}^2 + \sigma_{NEP}^2\right) + \frac{8}{\eta_d^4 \eta_h^2}\left(\sigma_{SN}^4 + \sigma_{NEP}^4\right) + \frac{16\sigma_{SN}^2 \sigma_{NEP}^2}{\eta_d^4 \eta_h^2} \tag{25}$$

which is also needed in Eq. (22). Combining the previous several equations yields

$$CNR = \frac{\left\langle N_L \tilde{N}_S \right\rangle}{\sqrt{\frac{4N_L N_S\left(\sigma_{SN}^2 + \sigma_{NEP}^2\right)}{\eta_d^2 \eta_h} + \frac{4\left(\sigma_{SN}^4 + \sigma_{NEP}^4\right)}{\eta_d^4 \eta_h^2} + \frac{8\sigma_{SN}^2 \sigma_{NEP}^2}{\eta_d^4 \eta_h^2}}} \tag{26}$$

Making the substitutions for the variances of the noises yields further simplification. The numerator requires special attention. Eq. (23) shows that there is a bias in the estimation of $N_L N_S$; however, this bias is subtracted off of the estimate given by Eqs. (14) and (15) by subtracting the noise floor in Eq. (10). By using Eqs. (14) and (15) as the estimates of N_L and N_S, the final carrier-to-noise ratio is

$$CNR = \frac{N_S}{\sqrt{\frac{2N_S}{\eta_d \eta_h} + \frac{1}{\eta_d^2 \eta_h^2} + \frac{4N_S \sigma_{NEP}^2}{\eta_d^2 \eta_h N_L} + \frac{4\sigma_{NEP}^2}{\eta_d^4 \eta_h^2 N_L} + \frac{4\sigma_{NEP}^4}{\eta_d^4 \eta_h^2 N_L^2}}} \tag{27}$$

The first two terms in the denominator are the result of only shot noise and match the CNR model in [8, 9]. The other terms in the denominator are the result of detector noise in which the value of σ_{NEP} needs to be derived for the specific detector being used. For the results presented here there are two dominant terms in the denominator: the first and third. These dominant terms are similar magnitudes, i.e.

$$O\left(\frac{2N_S}{\eta_d \eta_h}\right) \approx O\left(\frac{4N_S \sigma_{NEP}^2}{\eta_d^2 \eta_h N_L}\right) \tag{28}$$

The shot noise and detector noise are the same order of magnitude because the experimental setup discussed later is not photon limited. A photon limited system may not need to include the NEP effects in the CNR because $O(\sigma_{NEP}^2/N_L) \ll 1$ would be true [18].

The CNR value given in Eq. (27) can only be evaluated for a single range-bin. Recall that the number of signal photons was derived only for a single range-bin in Eq. (4), and the spectral bandwidth was only a single range-bin in Eq. (21). Since the ISAL image likely contains many range-bin, the CNR of each-range-bin must be evaluated separately and tallied in some manner. For later analysis the "Mean CNR" of the range-bins which are populated by the target is reported.

4. CONTRAST DEFINITION

A quality metric used here to quantify the image quality resulting from the PGA process is the contrast of the image defined as the difference between the mean foreground and mean background pixels divided by the standard deviation of the background pixels, i.e.

$$C = \frac{\frac{1}{N}\sum_{\forall \underline{x}\in\gamma} I(\underline{x}) - \frac{1}{M}\sum_{\forall \underline{x}\notin\gamma} I(\underline{x})}{\sqrt{\frac{1}{M}\sum_{\forall \underline{x}\notin\gamma} I^2(\underline{x}) - \left(\frac{1}{M}\sum_{\forall \underline{x}\notin\gamma} I(\underline{x})\right)^2}} \tag{29}$$

where N is the number of foreground pixels, M is the number of background pixels, and γ denotes the set of pixels in the foreground. The criterion for a pixel being in the foreground can be defined in many ways. Here we simply define a polygon around the region of the image which corresponds to the shape of the target as observed in a clear, high-power image. In all of the targets studied here these are simple elementary shapes, i.e. a rectangle or a circle. This method is acceptable for the analyses presented here because we have *a priori* knowledge of the target. When comparing images of the same target with varying transmitter output power, the polygon is defined for the highest transmitter power case and kept consistent for all other power levels. It is not redefined for the lower power images regardless of what the image looks like. This gives a consistent basis for comparison.

The goal of using the contrast metric is to look at the trend in the contrast versus the CNR. By looking at the trend, the CNR value where the contrast reaches unity can be defined as the operational threshold of the PGA algorithm. This definition is made because when the contrast decreases to unity the foreground pixels typically have a similar value as the background pixels. This means that even if PGA autofocuses correctly, the image is still not necessarily resolvable to an observer. The contrast is thus only presented as a diagnostic metric for the PGA. Its requirement of *a priori* knowledge of the target does not make it a suitable blind test metric.

5. EXPERIMENTAL SETUP

The system consists of a transmitter, heterodyne receiver, rotating target, data processing, and hardware controllers. The laser is a 1310 nm tunable laser which produces a chirped waveform. The details of producing the chirp are presented in a concurrent paper [19]. The laser beam is split sending 90% to the transmitter to illuminate the target and 10% to the receiver to act as the local oscillator. The optical path is shown in the schematic in Figure 1.

The transmitter in the system takes on two forms: one introduces atmospheric noise while the other does not. The simple transmitter illuminates the target with a collimated beam from a fiber tip and is shown in Figure 1. The other transmitter illuminates the target with a dynamic speckle pattern which simulates atmospheric disturbances incurred while illuminating a spaceborne object from the Earth's surface. The phase error in the beam is introduced by passing the light through a "phase wheel." The phase wheel is a 4 inch optical window with varying thickness which rotates to introduce a piston error over an area r_0. To simulate the atmosphere the beam is passed through the phase wheel with a beam diameter of $6r_0$. The result is not just a phase piston error but a speckle pattern which changes in time. The speckle pattern is produced and then reimaged onto the target. In sequence, the light from the fiber tip is collimated, truncated to FWHM, and then focused such that is passes through the phase wheel when it has a width of $6r_0$. The focal point, where the speckle pattern lies, is reimaged onto the target such that the average speckle is slightly larger than the target. This system is shown in Figure 2.

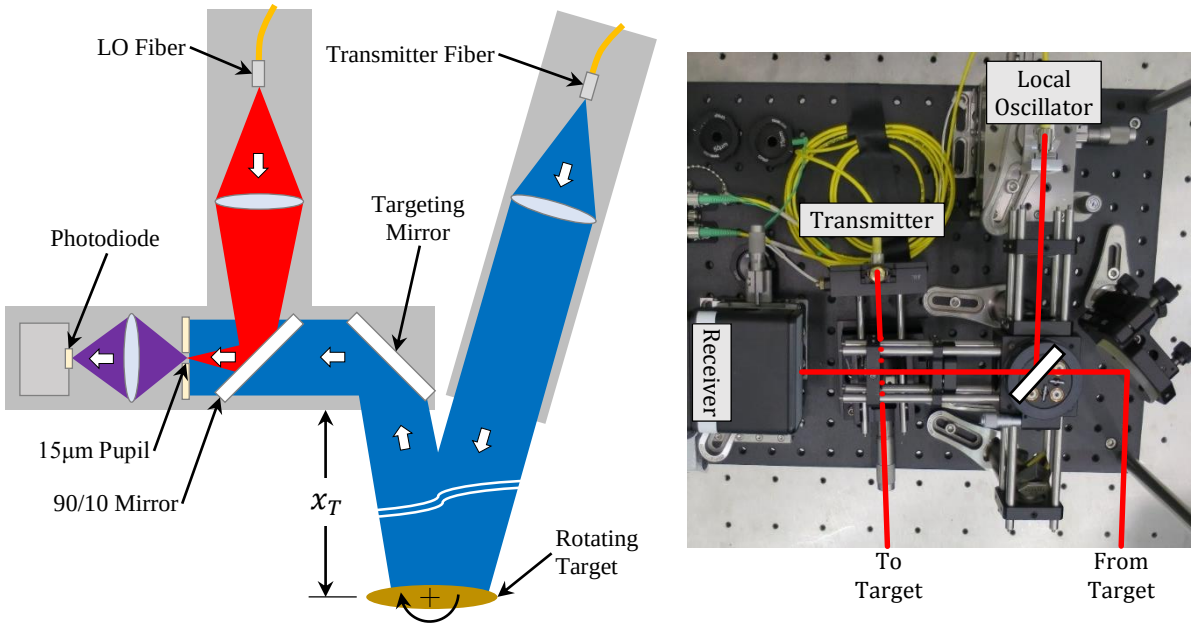

Figure 1. Imaging system schematic and photograph showing the simple transmitter and the heterodyne receiver.

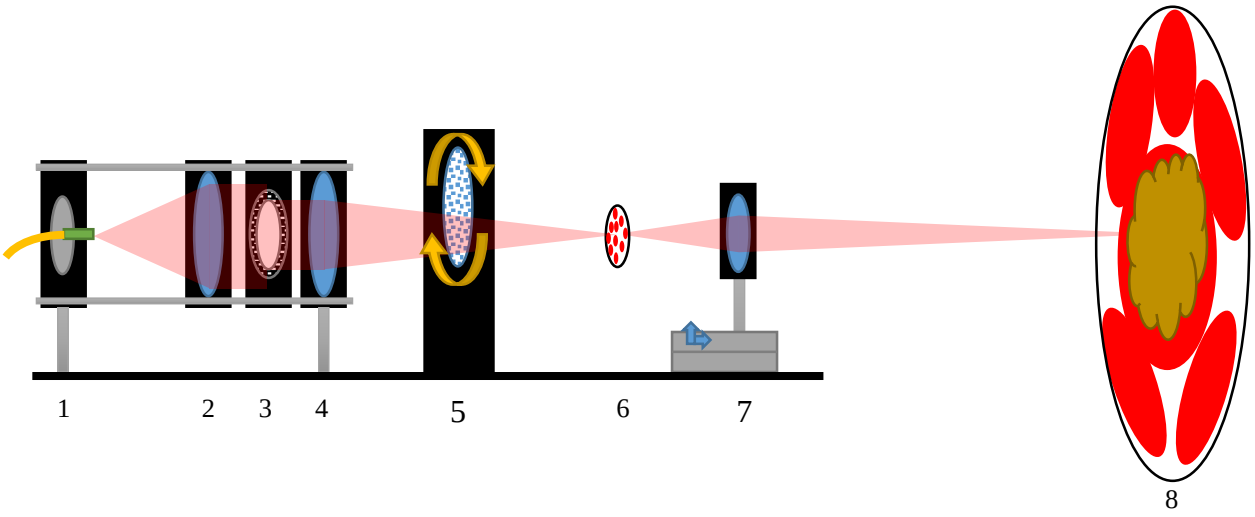

Figure 2. Schematic of the transmitter which introduces simulated atmospheric noise into the beam illuminating the target. (1) Fiber tip (2) Collimating lens (3) Iris (4) Focusing lens (5) Phase wheel (6) Speckle pattern (7) Reimaging lens (8) Speckle pattern on target

The target is a Spectralon plate mounted on a rotation stage which is actuated by a PZT shown in Figure 3. The rotation rate is 1.25e-5 rad/s for a 1 minute data collection period. Spectralon was chosen because it has nearly Lambertian behavior in the near IR [20]. This behavior is desirable because the target was oriented in two ways. The Spectralon surface normal was positioned at 45° azimuth 0° elevation and 0° azimuth 45° elevation relative to the incident beam. These two configurations are depicted in Figure 4. The blue highlighted region in the figure denotes the illuminated portion of the target and determines the shape of the observed image. The first case is denoted the "line" target, and the second case is denoted the "circle" target. These configurations were chosen because they represent two extremes. The line target has *few* cross-range-bins for each range-bin. The circle target has *many* cross-range-bins for each range-bin. It is expected that the contrast of the circle target's image will be less than the contrast of the line target's image because the values of the cross-range pixels in the image result from the Fourier transform of the pulse's Fourier transform. Therefore, Parseval's theorem dictates that for the same mean CNR the line target will have a higher contrast than the circle target.

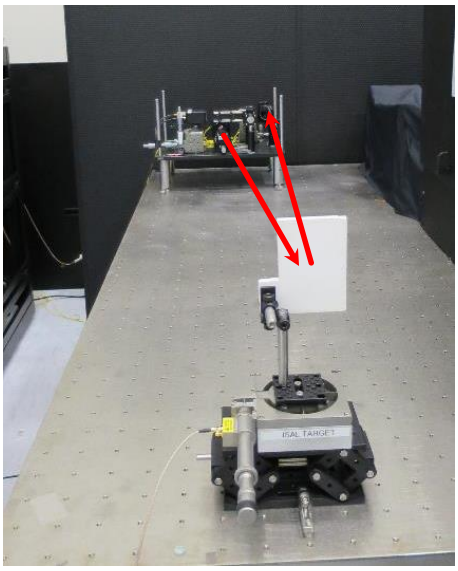

Figure 3. The imaging system as shown in Figure 1 and the Spectralon target on the PZT rotation stage.

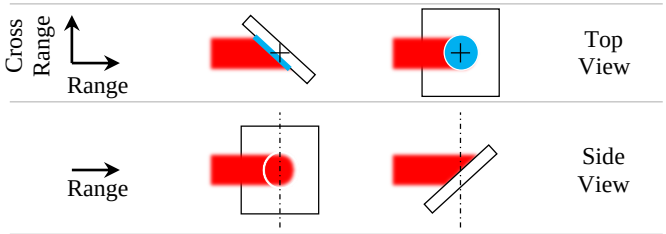

a) 45°-0° Line b) 0°-45° Circle

Figure 4. Orientations of the Spectralon target surface normal in azimuth-elevation relative to the illumination beam used for performance diagnostics. The axes shown in the side views denote the axis about which the target rotates. The blue region indicates the shape of the expected image in range and cross-range.

6. EXPERIMENTAL RESULTS

The experimental results demonstrate two main conclusions. The area target consistently has a lower contrast than the line target given the same CNR because the pixel values result from a Fourier transform in which Parseval's theorem must hold. Additionally, when atmospheric turbulence is introduced the image contrast decreases such that the minimum CNR which PGA will work increases. These conclusions were made by imaging the targets repeatedly while decreasing the transmitter power effectively reducing the CNR. The results are shown in Figure 5. Below a contrast of 1 the images were not resolved correctly. "Not resolved" means that the shape of the image foreground did not correspond to the target or the foreground was not distinguishable from the background noise. Without turbulence the line target was resolvable down to a CNR of 0.25 and the area target was resolvable down to a CNR of 0.4. Adding turbulence increased the minimum CNR for the line target to 0.6. Higher CNR measurements were not possible due to the power losses associated with the extra optics in the transmitter shown in Figure 2.

Images of the line and area targets without turbulence at high and low CNRs are shown in Figure 6 and Figure 7. Comparing the magnitude of the noise in the background confirms the difference in the contrast of the two images. In the low CNR image, the noise artifacts are nearly the same magnitude as the foreground. Figure 8 shows the line target at the lowest CNR dataset which revealed an image. Comparing with Figure 6b shows that for a similar contrast and quality of the image, the CNR is over twice as high. Detailed views of the photons and CNR per range bin for the line target at low CNR with and without turbulence are shown in Figure 9 and Figure 10. Without turbulence the image was recovered with as few as 1.5 photons per range-bin per pulse. With turbulence the number of photons per range-bin per pulse for image recovery is nearly doubled.

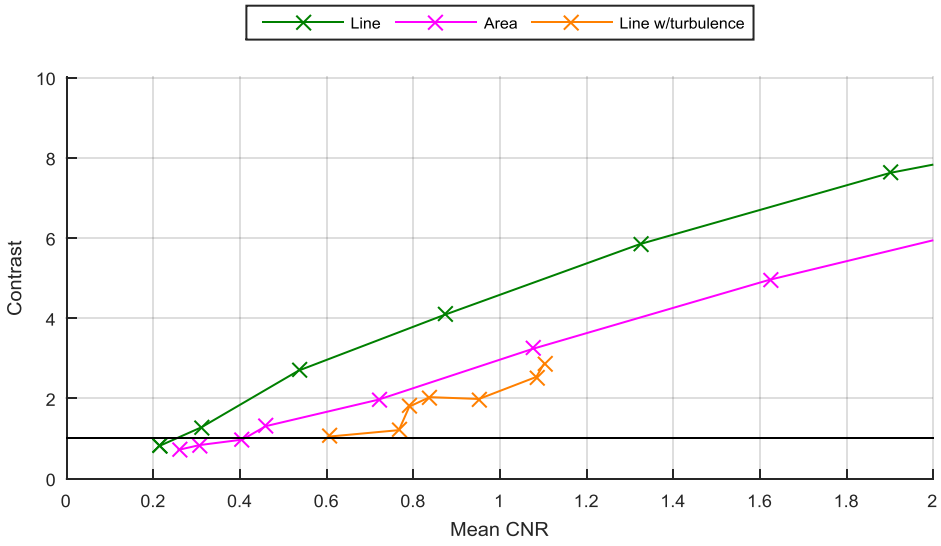

Figure 5. Contrast vs Mean CNR for the line target, area target, and the line target with atmospheric turbulence. The uncertainties of the Mean CNR values are ≤0.1.

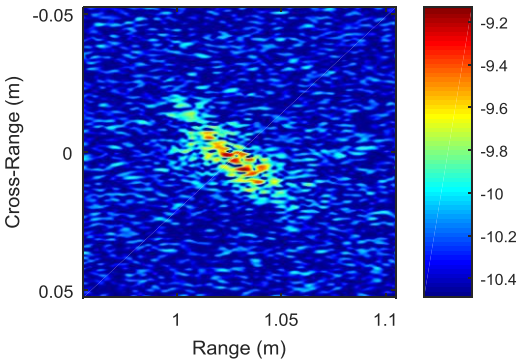

a) Mean CNR = 1.32, Contrast = 5.9

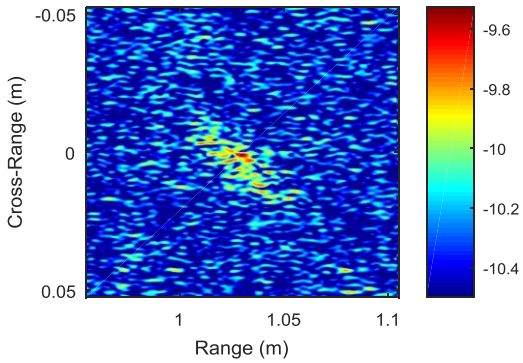

b) Mean CNR = 0.31, Contrast = 1.3

Figure 6. Sample high and low CNR images of the line target.

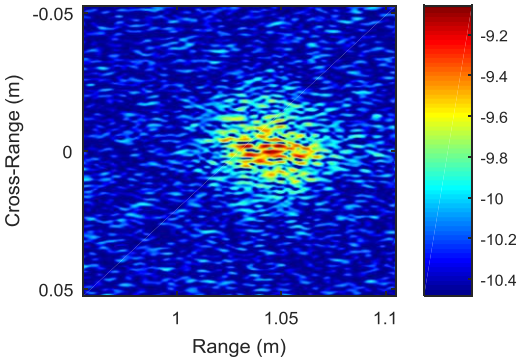

a) Mean CNR = 1.07, Contrast = 3.2

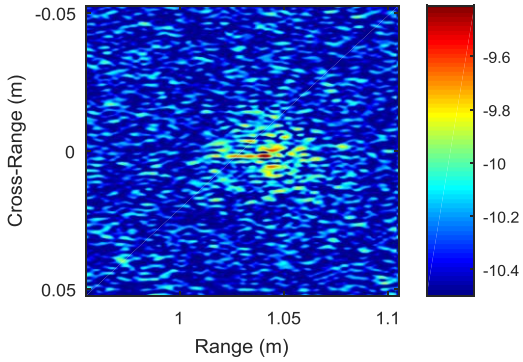

b) Mean CNR = 0.31, Contrast = 0.84

Figure 7. Sample high and low CNR images of the line target.

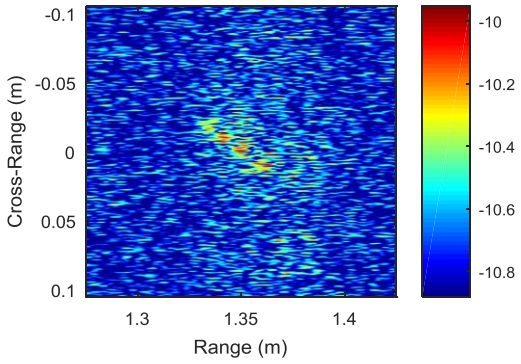

Figure 8. Image of the line target with atmospheric turbulence. Mean CNR = 0.79. Contrast = 1.8.

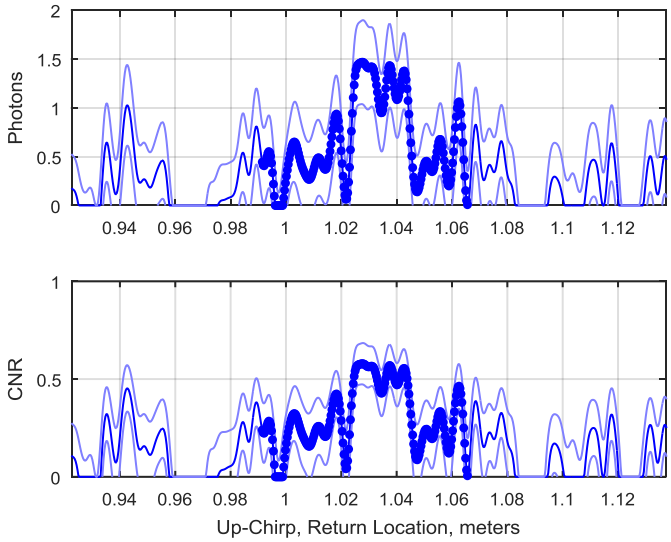

Figure 9. The photon counts and CNR per range bin for the image in Figure 6b. The highlighted region denotes the range-bins that correspond to the target according to *a priori* knowledge. The lighter lines denote the 1σ uncertainty bound.

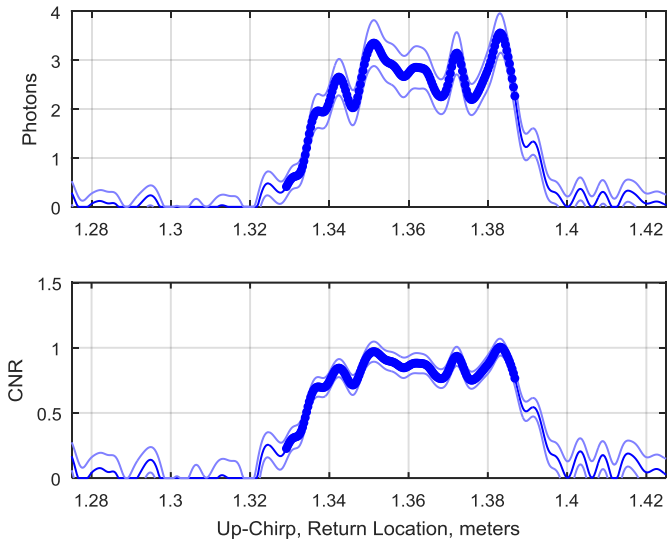

Figure 10. The photon counts and CNR per range bin for the image in Figure 8. The highlighted region denotes the range-bins that correspond to the target according to *a priori* knowledge. The lighter lines denote the 1σ uncertainty bound.

7. CONCLUSIONS

We presented an analytical model of the ISAL observation data which included the heterodyne process, photon noise, detector noise, and the pulse Fourier transformation to isolate the return signal in a single range-bin. This model was used to derive a CNR model similar to that used in telecommunications and other SAL studies. The inputs to this CNR model were derived based from the voltage measurements which would be available in an experiment. Next, a quality metric for the PGA image, the contrast, was presented. A comparison of the CNR to the contrast revealed a trend which indicates the failure threshold for the PGA.

Using the contrast quality metric to observe the PGA performance trend as the return signal strength was decreased revealed a consistent threshold where PGA would stop working in the absence of atmospheric turbulence. This threshold was expected and was observed to occur at a contrast level of approximately unity. This corresponds to ~1.5 photons per range-bin which is a Mean CNR of 0.25. This threshold represents a necessary condition—but not a sufficient condition—for PGA to work since most real-world data will have atmospheric turbulence. With the addition of atmospheric phase error in the illumination beam simulating observation of a near-Earth object from the ground, the Mean CNR threshold was increased to 0.6. It should be noted that when the PGA began to fail, often speckles in the image were visible above the background noise; however, the shape of the target was not resolved. This implies that there was sufficient return signal strength to separate signal from noise, but the phase information on which PGA relies was degraded.

The threshold number of photons of 1.5 for PGA to work (in the absence of atmospheric turbulence) can be attributed to the uncertainty principle relationship between the number of photons and the variance of the phase. While many theories and specialized analyses pertaining to heterodyne detection exist on the topic [21, 22, 23, 24, 25], essentially the phase variance $\Delta\varphi$ is related to the photon count N by a relationship like $\Delta\varphi \sim N^{-1/2}$ in [22]. This implies that as the photon count gets sufficiently small the variance of the phase increases to a point where sequential measurements of the phase cannot be unwrapped with adequate accuracy. Since PGA relies on the ability to phase connect the return signal across many pulses, a growth in the phase variance causes convergence of the PGA to be impossible due to the Heisenberg uncertainty. We thus suggest that improvements to the data processing algorithms, the experiment hardware, or the system parameters may not provide substantial improved performance in the ~1 photons per range-bin regime unless the phase variance can be reduced by considering many range-bins.

8. ACKNOWLEDGEMENTS

The research described in this paper was performed at the Jet Propulsion Laboratory of the California Institute of Technology under contract with the National Aeronautics and Space Administration and the Air Force Research Laboratory.

REFERENCES

[1] Barber, Z. W. and Dahl, J. R., "Synthetic aperture ladar imaging demonstrations and information at very low return levels," Applied Optics 53(24), 5531-5537 (2014).

[2] McManamon, P. F., "Review of ladar: a historic, yet emerging, sensor technology with rich phenomenology," Optical Engineering 51(6), 1-13 (2012).

[3] Luo, H., Yuan, X. and Zeng, Y., "Range accuracy of photon heterodyne detection with laser pulse based on Geiger-mode APD," Optics Express 21(16), 18983-18993 (2013).

[4] Andrews, A. K., Hudson, R. S. and Psaltis, D., "Optical-radar imaging of scale models for studies in asteroid astronomy," Optics Letters 20(22), 2327-2329 (1995).

[5] Harris, A. W., Young, J. W., Conteiras, L., Dockweiler, T., Belkora, L., Salo, H., Harris, W. D., Bowell, E., Poutanen, M., Binzel, R. P., Tholen, D. J. and Want, S., "Phase relations of high albedo asteroids: The unusual opposition brightening of 44 Nysa and 64 Angelina," Icarus 81(2), 365-374 (1989).

[6] Mishchenko, M. I. and Dlugach, J. M., "Coherent backscatter and the opposition effect for E-type asteroids," Planetary and Space Science 41(3), 173-181 (1993).

[7] Pellizzari, C. J., Bos, J., Spencer, M. F., Williams, S., Williams, S. E., Calef, B. and Senft, D.C., "Performance characterization of Phase Gradient Autofocus for Inverse Synthetic Aperture LADAR," IEEE Aerospace Conference, 1-11 (2014).

[8] Lucke, R. L. and Rickard, L. J., "Photon-limited synthetic-aperture imaging for planet surface studies planet surface studies," Applied Optics 41(24), 5084-5095 (2002).

[9] Lucke, R. L., Rickard, L. J., Bashkansky, M., Reintjes, J. and Funk, E. E., "Synthetic aperture ladar (SAL): Fundamental theory, design equations for a satellite system, and laboratory demonstration," Naval Research Laboratory, Washington DC, (2002).

[10] Gatt, P., Jacob, D., Bradform, B. and Krause, B., "Performance bounds of the phase gradient autofocus algorithm for synthetic aperture ladar," Proc. SPIE 7323, (2009).

[11] Falletti, E., Pini, M. and Presti, L., "Low complexity carrier-to-noise ratio estimators for GNSS digital receivers," IEEE Transactions of Aerospace and Electronic Systems 47(1), 420-437 (2011).

[12] Sharawi, M. S., Akos, D. M. and Aloi, D. N., "GPS C=N0 estimation in the presence of interference and limited quantization levels," IEEE Transactions of Aerospace and Electronic Systems 43(1), 227-238 (2007).

[13] Jiang, L. A. and Luu, J. X., "Heterdyne detection with a weak local oscillator," Applied Optics 47(10), 1486-1503 (2008).

[14] Winzer, P. J. and Leeb, W. R., "Coherent lidar at low signal powers: Basic considerations on optical heterodyning," Journal of Modern Optics 45(8), 1549-1555 (1998).

[15] Goodman, J. W., [Statistical Optics], Wiley, New York, (1985).

[16] Carrara, W., Majewski, R. and Goodman, R., [Spotlight Synthetic Aperture Radar: Signal Processing Algorithms], Artech House, Boston, (1995).

[17] Richards, P. L., "Bolometers for infrared and millimeter waves," Journal of Applied Physics 76(1), 1-24 (1994).

[18] Frenkel, A., Sartor, M. A. and Wlodawski, M. S., "Photon-noise-limited operation of intensified CCD cameras," Applied Optics 36(22), 5288-5297 (1997).

[19] Zhou, H., Nemati, B., Shao, M., Schulze, W. and Trahan, R., "Low-Cost Chirp Linearization for Long-Range ISAL Imaging Application," Proc. SPIE 9846, 13 (2016).

[20] Bhandari, A., Hamre, B., Frette, O., Zhao, L., Stamnes, J. and Kildemo, M., "Bidirectional reflectance distribution function of Spectralon white reflectance standard illuminated by incoherent unpolarized and plane-polarized light," Applied Optics 50(16), 2431-2442 (2011).

[21] Opatrny, T. "Number-phase uncertainty relations," Journal of Physics A: Mathematical and General 28(23), 6961-6975 (1995).

[22] Shapiro, J. H. and Shepard, S. R., "Quantum phase measurement: A system-theory perspective," Physical Review A 43(7), 3795-3818 (1991).

[23] Shapiro, J. H. and Wagner, S. S., "Phase and amplitude uncertainties in heterodyne detection," IEEE Journal of Quantum Electronics 20(7), 803-813 (1984).

[24] Perinova, V., Luks, A. and Perina, J., [Phase in Optics], World Scientific Publishing, Singapore, (1998).

[25] Carruthers, P. and Nieto, M. M., "Phase and angle variables in quantum mechanics," Reviews of Modern Physics 40(2), 411-440 (1968).